An elastic–plastic-cracking model for finite element analysis of indentation cracking in brittle materials

W. Zhang, G. Subhash *

Department of Mechanical Engineering-Engineering Mechanics, Michigan Technological University, 1400, Townsend Drive, Houghton, MI 49931, USA

Abstract

An 'elastic–plastic-cracking' (EPC) constitutive model was developed and incorporated into the commercial explicit finite element package ABAQUS to analyze the fracture characteristics of brittle materials subjected to indentation loads. The analysis indicated that the EPC model can capture the development of median cracks during the loading phase and the development of lateral cracks during the unloading phase of the Vickers indentation cycle. The influence of material properties on induced damage zone characteristics was analyzed by defining a non-dimensional brittleness parameter. The model predictions of hardness as well as load–depth (P–h) relationship during an indentation cycle were found to agree well with the experimental trends presented elsewhere in the literature. © 2001 Elsevier Science Ltd. All rights reserved.

Keywords: Vickers indentation; Brittle cracking model; Hardness; Brittleness

1. Introduction

Static indentation fracture mechanics approach has been widely used in the literature to evaluate the fracture characteristics of brittle materials (Lawn et al., 1980; Chiang et al., 1982; Ponton and Rawlings, 1989a,b; Cook and Pharr, 1990; Zeng et al., 1996). In these investigations it has been well established that radial and median cracks develop normal to the specimen surface during loading of the indenter and lateral cracks develop parallel to the surface during unloading of the indenter as illustrated schematically in Fig. 1. These investigations have also revealed the existence of a plastic region directly beneath the indenter (Cook and Pharr, 1990). Plastic flow under hydrostatic conditions and compressive loads has been observed in glasses and ceramics by various researchers (Marsh, 1964; McClintock and Argon, 1966; Schinker and Doll, 1982; Spur et al., 1985; Subramanian and Keat, 1985; Inasaki, 1986; Subhash and Nemat-Nasser, 1993; Lankford et al., 1998). In the case of indentation experiments, the large compressive stresses which occur directly beneath the indenter can induce plastic deformation during the loading phase and allow for residual stress development during the unloading phase resulting in lateral cracking parallel to the surface.

---

* Corresponding author. Tel.: +1-906-487-3161; fax: +1-906-487-2822.
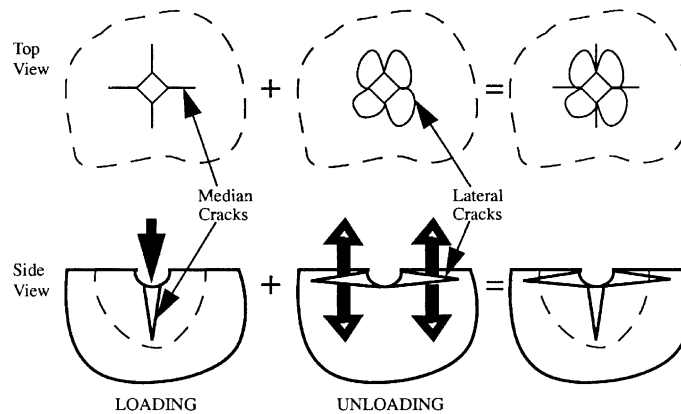*E-mail address:* subhash@mtu.edu (G. Subhash).

Fig. 1. Schematic of the crack systems that evolve during loading and unloading phases of a Vickers indentation cycle.

To describe this cracking process, several analytical models have been proposed in the literature (Lawn et al., 1980; Chiang et al., 1982; Ahn et al., 1998). In these models, the elastic stress field due to a point load on a semi-infinite space have been superposed on the plastic stress field due to an expanding cavity to determine the stress required to cause the observed crack patterns. The expanding cavity model, originally proposed by Yoffe (1982), is capable of capturing the residual stress fields upon unloading of the indenter and the lateral crack development.

Numerical models using finite element (FE) methods have also been used to analyze the indentation fracture characteristics of brittle materials (e.g. Liaw et al., 1984). Such models fail to capture the lateral crack development upon unloading because of the lack of plastic zone beneath the indentation. Elastic–plastic behavior of metals and ceramics under indentation loads have been extensively studied using FE method by Giannakopoulos et al. (1994), Larsson et al. (1996), Zhang and Mahdi (1996), Zeng et al. (1996), Care and Fischer-Cripps (1997), Fischer-Cripps (1997), and Marx and Balke (1997). However, these analyses mainly focussed on the stress field development and the prediction of crack's initiation but not on the crack evolution during the indentation process. Larsson (1995) presented a fictitious crack model based on plastic localization and the subsequent discontinuity. Such a model, however, is difficult to incorporate into a commercial FE package since discontinuity is not taken into account in most commercial packages. Chow et al. (1993) proposed an incremental form of elastoplastic theory coupled with anisotropy damage model for fracture evolution in brittle solids. This model has the advantages of a clear physical representation of the brittle fracture and is relatively simple to incorporate into a FE code, but the damage evolution laws are difficult to obtain.

In this paper, an 'elastic–plastic-cracking' (EPC) constitutive model is presented for isotropic brittle materials. In the EPC model, the elastic–plastic response of a material is followed by a smeared cracking process. The advantages of this model are that its parameters are easier to estimate or obtain from the existing literature and it is easy to implement in commercial FE packages. In the current work, the model has been successfully incorporated into the explicit ABAQUS FE code (version 5.8) (ABAQUS, 1998a,b) using the user subroutine VUMAT (see ABAQUS user manual) to investigate the evolution of various crack systems during loading and unloading phases of the Vickers indentation cycle.

2. Model formulation and implementation

The EPC constitutive model, illustrated in Fig. 2(a), consists of a traditional bilinear elastic–plastic response OAB followed by a crack opening process BC along which the stress is released due to cracking.

The unloading process from an arbitrary point along the path BC is denoted by DE. Since cracking results in degradation of shear modulus, the slope of DE is considered to be lower than that of OA. The modulus degradation occurs according to the current crack opening displacement (COD) as will be described later.

During plastic deformation, the Mises yield surface can be written as

$$f(\sigma, \sigma_e) = \frac{3}{2} S : S - \sigma_e^2(\varepsilon_e^p) = 0, \tag{1}$$

where, S is the deviatoric stress matrix, σ_e is the equivalent yield stress given by

$$\sigma_e = Y + E_p \varepsilon_e^p, \tag{2}$$

where, Y is uniaxial yield stress, E_p is plastic hardening modulus and ε_e^p is the equivalent plastic strain defined as

$$\varepsilon_e^p = \int_0^t \sqrt{\frac{2}{3} \dot{\varepsilon}^p : \dot{\varepsilon}^p} \, dt. \tag{3}$$

The total strain rate is decomposed into elastic and plastic parts as

$$\dot{\varepsilon} = \dot{\varepsilon}^e + \dot{\varepsilon}^p. \tag{4}$$

The stress rate is related to the elastic strain rate by Hooke's law

$$\dot{\sigma} = \lambda \text{trace}(\dot{\varepsilon}^e) I + 2\mu \dot{\varepsilon}^e, \tag{5}$$

where λ and μ are Lame constants I is the identity matrix. The plastic strain rate is given by the normality condition

$$\dot{\varepsilon}^p = \dot{\gamma} \frac{\partial f}{\partial \sigma}, \tag{6}$$

where, the scalar $\dot{\gamma}$ can be determined with the commonly used elastic predictor, radial return algorithm.
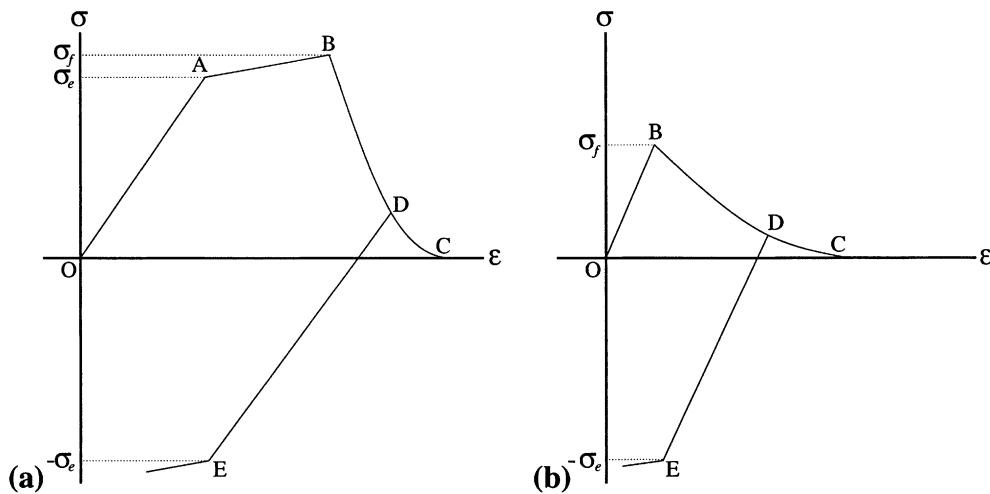

Fig. 2. (a) Generalized elastic–plastic-cracking constitutive model and (b) reduced model applied to brittle materials.

The crack initiation is assumed to occur according to the Rankine criterion which states that a crack is formed when the maximum principal tensile stress exceeds the tensile strength of a brittle material. To account for the intensity of damage, a maximum three cracks are allowed to occur at any given material point. When the maximum principal stress at a given material point exceeds the predefined fracture stress σ_f, a mode I crack would appear in a direction normal to that of the maximum principal stress axis. At the same material point, a second crack could occur only if the maximum tensile stress in the first crack's plane exceeds σ_f and a third crack could occur only if the tensile stress in a direction perpendicular to both of the above crack normals exceeds σ_f. The normals to the three cracks form a local orthogonal coordinate system as indicated by the prime axes in Fig. 3. Once a crack appears, its direction does not change, and hence this is called a 'fixed orthogonal crack model'.

Let T be the transformation matrix from the global to the local coordinate system. The local stress matrix t and strain matrix e can be obtained from the global (applied) stress and strain values as

$$t = \begin{bmatrix} t_1 & t_{12} & t_{13} \\ t_{12} & t_2 & t_{23} \\ t_{13} & t_{23} & t_3 \end{bmatrix} = T\sigma T^{\mathrm{T}} \qquad e = \begin{bmatrix} e_1 & e_{12} & e_{13} \\ e_{12} & e_2 & e_{23} \\ e_{13} & e_{23} & e_3 \end{bmatrix} = T\varepsilon T^{\mathrm{T}}. \tag{7}$$

The normal stress t_i across a given crack i will be updated when it exceeds the current fracture stress, which is assumed to be a power law function of the COD u_i given by

$$t_i = \sigma_f f_i \quad (i = 1, 2, 3), \tag{8}$$
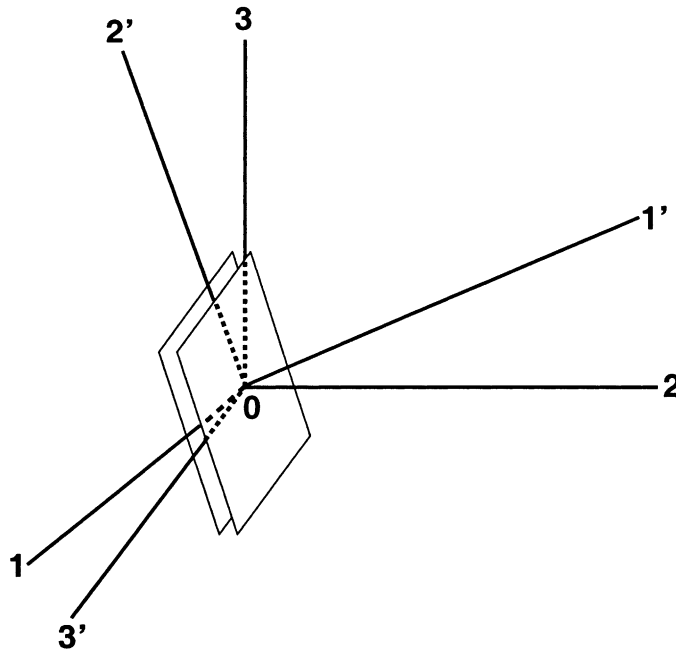
where

$$f_i = (1 - u_i/u_0)^n, \tag{9}$$

Fig. 3. Illustration of local and global coordinate systems.

σ_f is the uniaxial fracture stress, u_0 and n are assumed to be material constants. In this paper, u_0 is assumed to be the maximum COD and is taken to be 5 μm. This value is consistent with the experimental observations of Yu and Kobayashi (1993) on ceramic matrix composites. The parameter n controls the shape of the post-cracking (stress release) curve illustrated in Fig. 4 and is assumed to be parabolic in nature with $n = 2$.

The COD u_i is difficult to obtain and hence we estimate u_i by multiplying the cumulative cracking strain e_i by a characteristic length h, i.e.,

$$u_i = he_i = h \int de_i, \tag{10}$$

where, h is the cube root of the corresponding element volume, and de_i is the incremental strain between two adjacent time steps during the cracking process at a given material point. Once COD is calculated for a given crack, the total damage magnitude at a given material point is calculated and plotted by defining the effective COD u_d along the three orthogonal directions, i.e.,

$$u_d = \sqrt{u_1^2 + u_2^2 + u_3^2}. \tag{11}$$

The shear stresses on a crack plane will also be released to zero when the crack is opening. To simplify the model, we assume the effective shear modulus G to be a function of the corresponding post-cracking functions f_i and f_j (see Appendix A) in two orthogonal directions, i.e.,

$$G = \frac{\mu f_i f_j}{f_i + f_j - f_i f_j} \quad (i \neq j), \tag{12}$$

where μ is the shear modulus of the uncracked material. Thus, in the local coordinate system, shear stress t_{ij} can be expressed as a function of the sum of the elastic and cracking strains, i.e.,
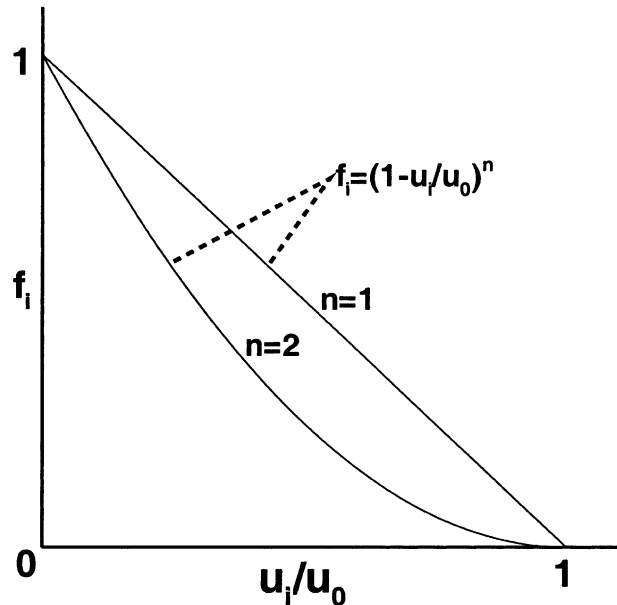

Fig. 4. Illustration of post-cracking function f_i versus normalized COD in local coordinate system.

$$t_{ij} = 2G(e_{ij}^e + e_{ij}^c) = 2G(e_{ij} - e_{ij}^p). \tag{13}$$

The above two equations are derived in the appendix. Note that the shear stress is not defined as a function of cracking strain alone (as done in ABAQUS) and hence the shear modulus remains finite even when the cracking strain tends to zero. Stresses will be rotated back to global system after they are updated in the local system in order to calculate new strains and displacements in the global coordinate system.

It should be emphasized here that there is no macrocrack being tracked in our model. The macrocrack can be viewed as the adjoining smeared microcrack system, i.e., a set of materials points forms the macrocrack similar to the concept of crack growth described by the elastic-cracking model in ABAQUS (version 5.8) theory manual. However, the current model differs from the elastic-cracking model available in ABAQUS in several ways. *First*, the introduction of plasticity allows for residual stress development and lateral cracking upon unloading during the indentation process. *Second*, the crack strain is not isolated from the total strain. In our model, stresses are assumed to relax to zero as per the relationship between stress and estimated COD (Eqs. (8)–(10) and (12)–(13)). Therefore, the model eliminates the need for defining the relationship between stress and pure crack strain, which can cause over stiffening of the modulus associated with cracking strain (as is currently done in ABAQUS) because the modulus tends to infinity as the crack strain approaches to zero (see Eq. (A.1) in Appendix A). *Third*, the model considers permanent strain associated with cracking even when the crack is completely closed. This is achieved by considering the shear modulus degradation as per the Eq. (12).

3. Model verification

To verify the above EPC constitutive model, a uniaxial tension–compression test was performed on a single element ceramic material. The properties of the material are presented in Table 1. Although the above EPC model illustrated in Fig. 2(a), can capture a wide range of material behavior, when applied to brittle materials (that have a yield stress greater than the fracture stress) the model is reduced to that shown in Fig. 2(b). It has been well established that brittle materials exhibit only elastic response prior to cracking during tensile loading and plastic deformation (without cracking) during compressive loading. Also, the compressive yield stress is considerably greater than the tensile fracture stress. Accordingly, the compressive yield strength is assumed to be 10 times greater than the tensile fracture stress. This assumption is valid for typical brittle materials which exhibit fracture during tensile loading and plastic response during compressive loading.

Fig. 5(a) illustrates the applied strain–time curve OABC to the test element. Fig. 5(b)–(d) are the results obtained from the model. In Fig. 5(b), the stress–time plot reveals that although the strain increases linearly up to the point A in Fig. 5(a), the stress increases linearly only up to the fracture stress of 0.5 GPa. This response is indicated by the line OA′ in Fig. 5(b). Upon fracture, the stress is released along A′A as per the post-cracking function f (Eq. (9)). The subsequent unloading (AB in Fig. 5(a)) results in a linear response along AB′. Since the ceramic is assumed to reveal plastic response only during compression, once the compressive stress exceeds the yield stress (5 GPa) the element exhibits plastic response with hardening along B′B. Upon reversing the strain path (along BC in Fig. 5(a)), the stress follows the elastic response along BC′, where, C′ refers to the maximum permissible tensile stress (same as A in Fig. 5(b)) for the

Table 1
Material properties

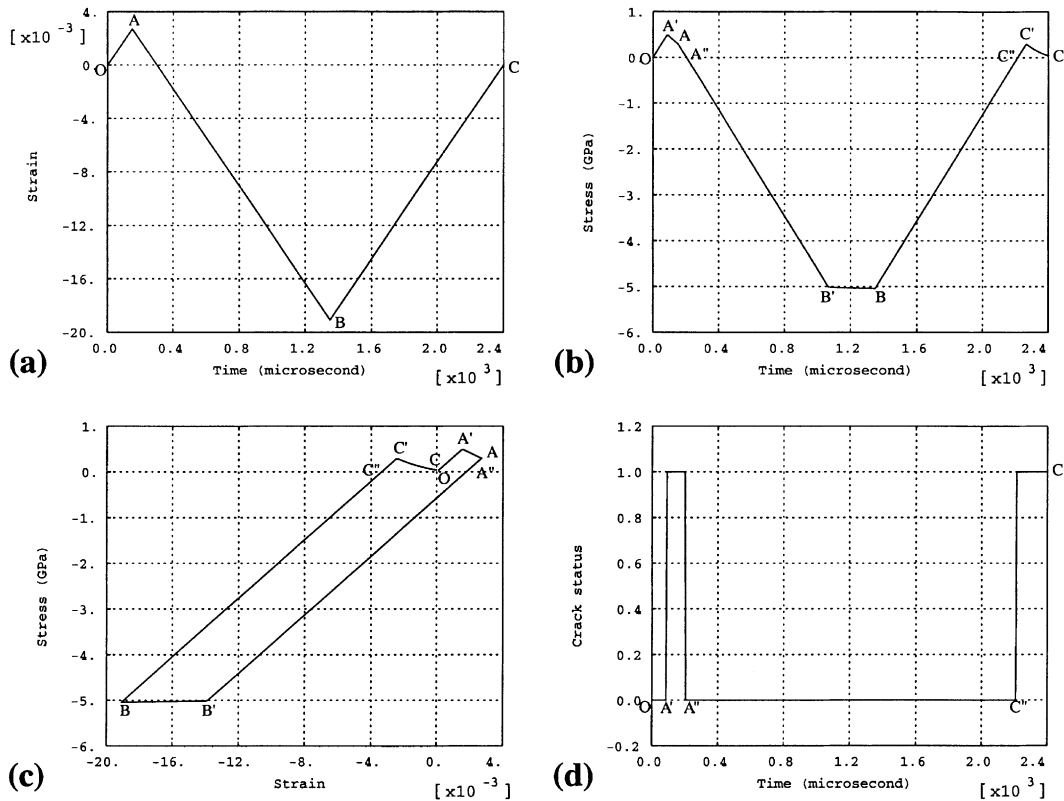| ρ (g/cm^3)	E (GPa)	v	Y (GPa)	E_p (GPa)	σ_f (GPa)
3.2	320	0.24	5	3.2	0.5

Fig. 5. Single element tension–compression test results. (a) Strain–time curve, (b) stress–time curve, (c) stress–strain curve and (d) crack status versus time.

cracked material. Finally the material unloads along C'C. The combined stress–strain response of the material is illustrated in Fig. 5(c). The crack status at various times during the loading and the unloading cycle is indicated in Fig. 5(d). In the absence of a crack or whenever the crack is closed, the status is indicated as zero and when the crack is open the status is indicated as one. Note that the crack assumes the value one when the stress exceeds the current fracture stress and remains tensile between A' and A" and again when the stress is tensile between C" and C.

Since the above numerical experiment, based on the EPC constitutive model, seems to capture the basic features of deformation in a brittle material subjected to a simple uniaxial loading, the model is applied to investigate the fracture evolution characteristics of brittle materials subjected to Vickers indentation loads. The relative influences of material properties on the evolution of damage zone size during Vickers indentation are reported in the following section.

4. Vickers indentation

Cylindrical specimens of 5 mm in diameter and 2.5 mm in length were used for finite element discretization. Due to the symmetry of the problem, only one-fourth of the specimen was modeled as 5376 hexahedral solid elements. Symmetric boundary conditions were applied to the two end planes. The bottom plane of the specimen was constrained in axial direction. To reduce computational time, a finer mesh

(12.5 μm) was adopted near the indentation region and a coarser mesh at distances farther away. To avoid numerical instability that may arise due cracking and the associated behavior, the recommended time step (automatically determined by ABAQUS) was further reduced by 1/3rd. It was found that this time-step always ensured convergence of the solution. The FE model is shown in Fig. 6. The Vickers indenter was modeled as a rigid body with five shell elements. The whole indenter was modeled for the purpose of visualization. The indenter was allowed to penetrate the specimen axially at a constant acceleration as described by the velocity versus time curve shown in Fig. 7, which results in a maximum indentation depth of 25 μm. The combined loading and unloading time duration was limited to 3 μs to minimize the computational time. The contact between the indenter and the specimen was assumed frictionless since friction is found to have no significant influence in indentation events (Giannakopoulos et al., 1994). Average CPU time for this problem was about 10 h on the SGI Origin 2000 supercomputer at University of Illinois at Urbana-Champaign (UIUC).

4.1. Indentation fracture morphology

Fig. 8(a) and (b) illustrate the induced damage u_d (see Eq. (11)) in a brittle material at a time corresponding to the peak indentation depth (1.5 μs) and upon complete unloading (3.0 μs), respectively. Notice that the model is capable of capturing the median crack (L_m) development during the loading phase and lateral crack (L_l) development during unloading phase. Fig. 9 illustrates the evolution of this damage zone size during an indentation cycle. It can be seen that the median crack develops only during the loading phase reaching a maximum just before the loading phase ends and remains constant thereafter. On the other hand, considerable lateral crack growth occurs during the unloading phase. These results are consistent with the observations of evolved crack patterns on borosilicate, fused-silica and magnesium oxide by
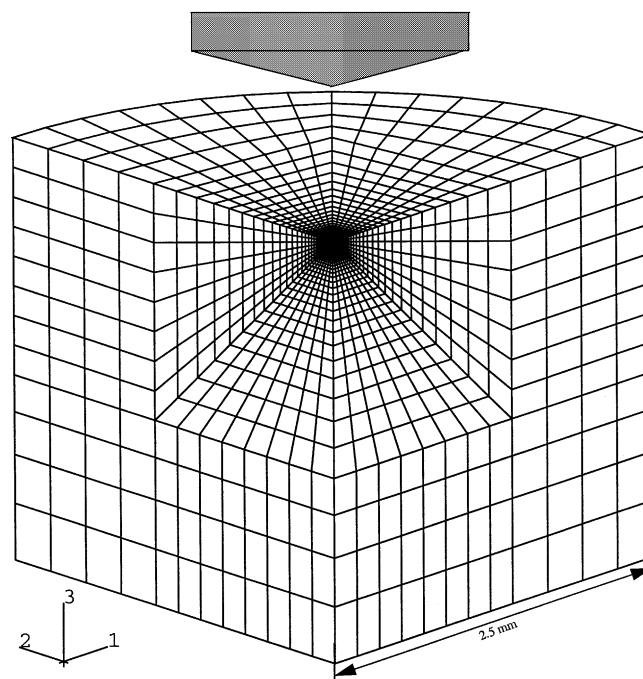

Fig. 6. Finite element discretization of the specimen and the indenter.
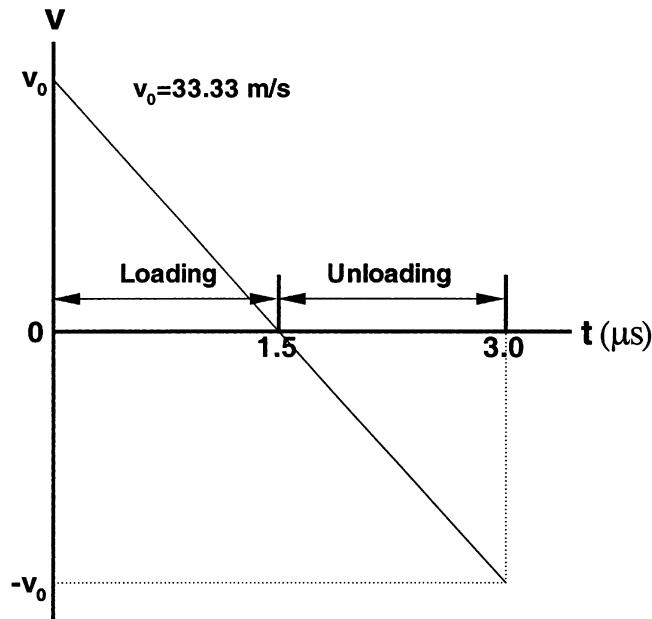
Fig. 7. Indenter velocity versus time during the indentation process.

Cook and Pharr (1990). While interpreting the results in Fig. 9(b), it should be cautioned that the measured lateral crack dimension (L_l) includes those elements that lie directly beneath and in contact with the indenter and undergo severe deformation as the indentation depth increases. Therefore, the damage zone size appeases to increase during the loading phase, because it is measured from the center of the indentation imprint. However, during unloading damage occurs in those elements that are not contact with the indenter and accordingly the lateral damage zone size grows as indicated in the figure.

Figs. 10(a) and (b) illustrate the contours of residual equivalent plastic strain at the end of the indentation cycle and the evolution of plastic zone size (L_p) during the indentation cycle, respectively. The plot in Fig. 10(b) clearly reveals that the plastic zone develops during the loading phase only. The creation of this plastic zone gives rise to the residual stress development during the unloading phase and leads to lateral cracking. This point is better illustrated in Figs. 11(a) and (b) where, the contours of maximum principal stress are plotted at the end of loading and unloading phases, respectively. Notice that compressive stresses in excess of yield stress (−5 GPa) are developed in the central region of the indentation and tensile stresses in excess of fracture stress (0.5 GPa) are developed along the periphery of this zone. On the other hand, during the unloading phase, large tensile stresses in excess of fracture stress are induced closer to the surface as well as in the regions surrounding the plastic zone resulting in lateral crack growth. Since the lateral crack development occurs parallel to the loading surface and at 45° to the Vickers indentation diagonals (see Fig. 1), it is informative to see the evolution of tensile stresses on planes closer to the surface and perpendicular to the z-axis (axis of the cylindrical specimen). Fig. 12 illustrates the evolution of tensile stresses on planes ($Z = -1, -10, -20, -30$ µm) at various times during the indentation cycle. Observation of these stresses reveals that the tensile stresses rise dramatically just after the unloading phase begins (Fig. 12(c)) indicating the lateral crack development. Notice that the magnitude of the tensile stress exceeds the fracture stress in these plots. This is because, cracking may have already occurred on planes other than z-plane and our model allows for cracking only in directions perpendicular to the existing cracks and hence, it is not necessary for stresses on z-planes to be less than the fracture stress. This is a major limitation of the proposed 'fixed orthogonal crack model'.
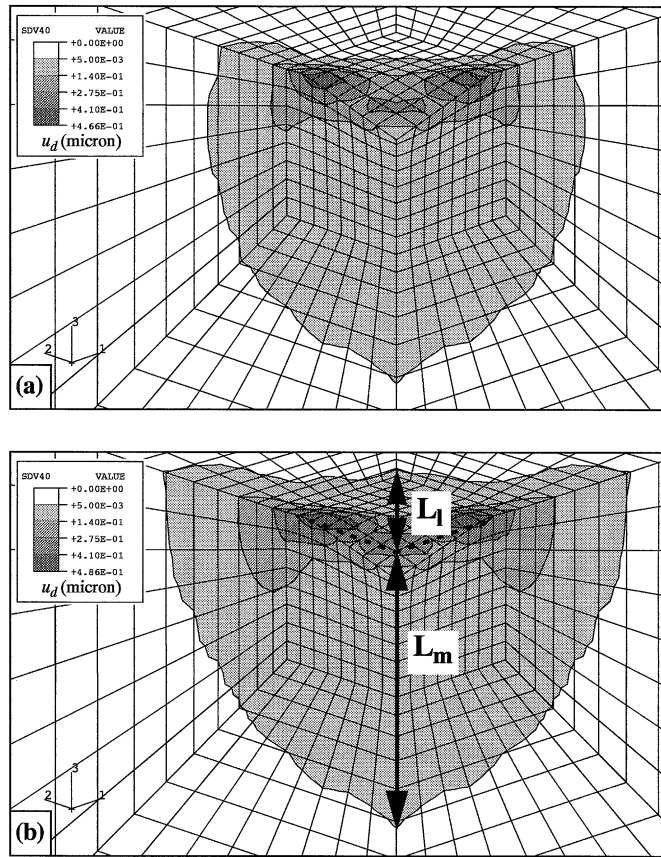
Fig. 8. The evolved damage zone size (u_d) at (a) the end of loading phase at 1.5 μs revealing the development of median cracks, and (b) upon complete unloading at 3.0 μs revealing the development of lateral cracks.

4.2. P–h relationships

Depth sensing indentation techniques have been recently (Bhattacharya and Nix, 1988; Cook and Pharr, 1990; Giannakopoulos et al., 1994; Zeng et al., 1996) gaining popularity due to their ability to provide load versus depth (*P–h*) curves which can be used to determine the mechanical properties such as hardness, modulus and fracture toughness of brittle materials. Zeng et al. (1996) made a rigorous analysis of Vickers indentation *P–h* curves using FE method and compared them to the experimentally obtained response by Cook and Pharr (1990). However, their analysis was limited to loading part of the curve and the unloading portion was not fully analyzed. In the investigations of Vickers indentation by Giannakopoulos et al. (1994) only compressive stress–strain response was utilized for FE model verification of *P–h* relationship. This approach may not be suitable for brittle materials because of the dominance of elastic deformation followed by tensile cracking. Since the EPC model can explicitly account for tensile cracking and compressive yielding, the analysis was extended to analyze the *P–h* response of brittle materials by varying the relevant material properties.

Figs. 13(a)–(c) reveal the computed *P–h* curves during the Vickers indentation cycle when one of the material properties is varied. In these calculations the maximum depth of indentation is kept constant at
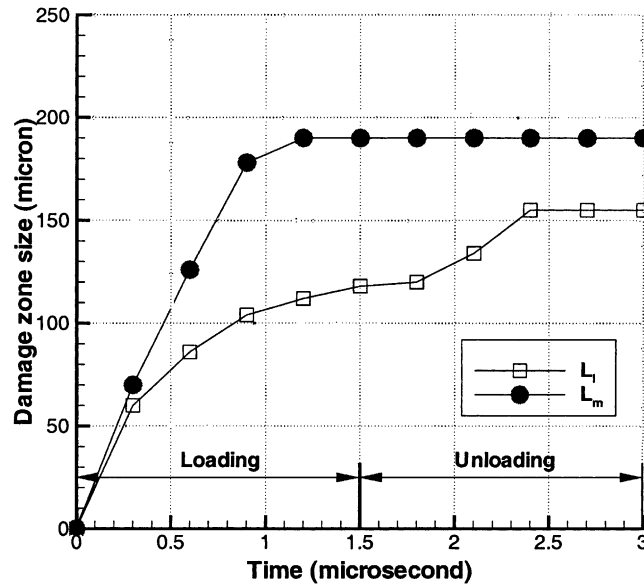
Fig. 9. Evolution of median and lateral damage zones during the indentation cycle.

25 μm. The analysis indicated that, as expected, an increase in Young's modulus increases the load required to achieve the same depth of penetration (Fig. 13(a)) but decreases the elastic recovery during the unloading phase, consistent with the experimental trends observed by Zeng et al. (1996). Similarly, an increase in the yield stress increases the load and the elastic recovery for the same depth of penetration as shown in Fig. 13(b). On the other hand, the fracture stress has almost no influence on the P–h relationship as indicated in Fig. 13(c). This is because P–h relationship is mostly an indication of elastic and plastic response of a material and accordingly the model predicts little effect when the fracture stress is varied. This result also agrees with Cook and Pharr's observations (1990) on different glasses and ceramics. The above results are summarized in Fig. 13(d) where it is noted that the elastic recovery is a non-linear function of Young's modulus and yield stress.

Although the above analysis clearly reflects the behavior of a ceramic when subjected to indentation loads, it is more useful to find a linear relationship between the elastic recovery and a parameter that includes easy to obtain material properties such as, Young's modulus and yield stress. Such a relationship can assist in development of empirical relationships that are useful for assessment of material property influences under varying experimental conditions. Lawn and Howes (1981) found that elastic recovery is a function of the ratio of hardness to elastic modulus. Our analysis revealed that elastic recovery is a linear function of $(Y/E)^{3/5}$ as shown in Fig. 14.

4.3. Hardness

Indentation hardness is one of most commonly used material properties by researchers and engineers. For metals, static indentation hardness has been related to yield stress according to the Tabor's (1951) relationship $H = 3Y$ (at 8% strain). Koeppel and Subhash (1999) found that the dynamic hardness and dynamic yield stress (at a strain rate 2000/s) also follow a similar relationship when the indentation durations were of the order of 100 μs. For ceramics, however, such a relationship between hardness and yield
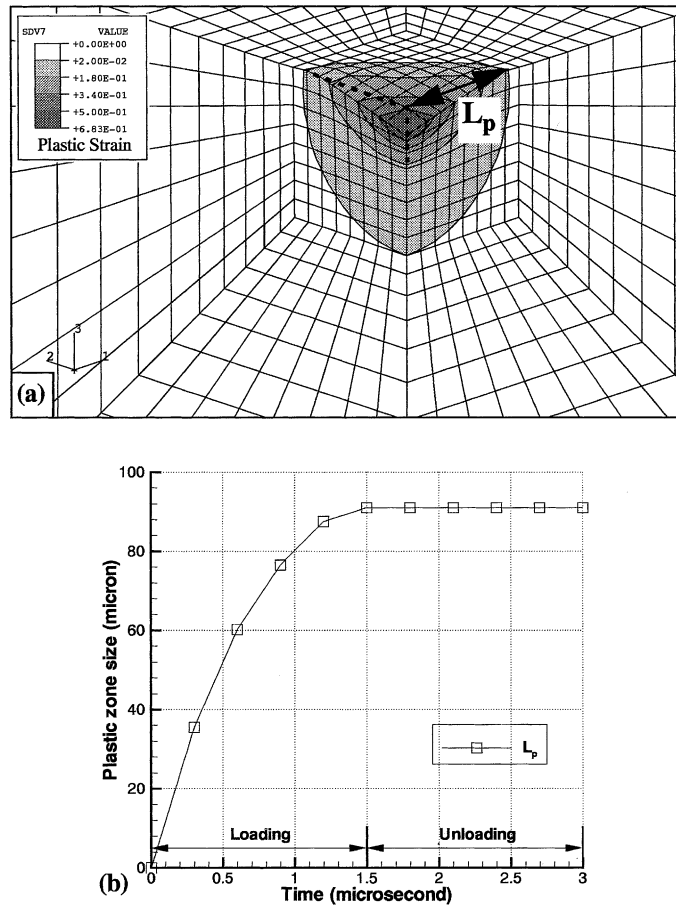
Fig. 10. (a) Plastic zone size at 3.0 μs and (b) evolution of plastic zone size during the indentation cycle.

stress can not be realized due to the absence of significant plasticity (Anton and Subhash, 2000). Lankford et al. (1998) rationalized the reasons for the lack of a direct correlations between the yield stress and hardness in ceramics and found that before plasticity can initiate in ceramics, the stress concentration associated with the dislocation generation can initiate microcracks. In the absence of well defined slip planes for dislocation motion (or continued plasticity) fracture continues to propagate leading to complete fragmentation of the ceramic.

Numerical analysis, on the other hand, can assist in identifying the relationship between hardness and material properties of ceramics. Such relationships are useful for formulation of empirical models or identification of difficult to obtain material properties. By systematic variation of material properties in the EPC model, the following expression for Vickers hardness H was determined,

$$H = (EY^3)^{1/4}. \tag{14}$$

A plot of H versus $(EY^3)^{1/4}$ reveals a linear relationship as presented in Fig. 15 where, the Vickers hardness was calculated as per (Tabor, 1951)
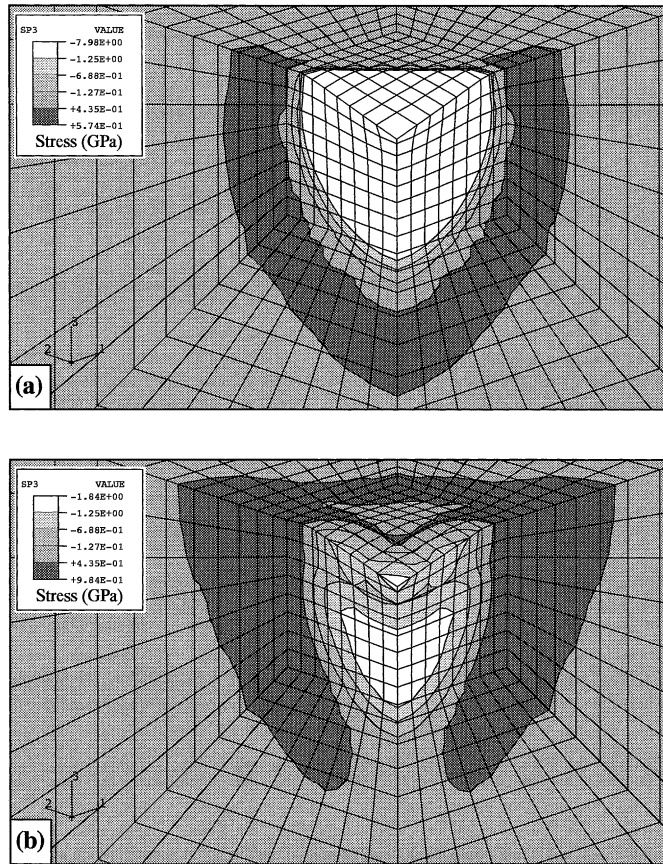
$$H = 1.8544(P/d^2), \tag{15}$$

Fig. 11. Maximum principal stress distribution at (a) at the end of loading phase at 1.5 μs, and (b) upon complete unloading at 3.0 μs.

where, P is the peak load of the indenter and d is the diagonal length of the contact impression in the FE simulations.

Since yield stress for ceramics is difficult to obtain, we verify the validity of the above relationship (Eq. (14)) by comparing the available data from the literature. In Table 2, the first two columns present the data on Young's modulus (E) and the hardness (H) of several brittle materials taken from Cook and Pharr (1990). The next two columns, hardness H' and yield stress Y', are the results obtained from the FE analysis of indentation process by Zeng et al. (1996). Notice that there is a good agreement between the simulations and the experiments on hardness values and therefore, the yield stress value Y' is taken as the reference for our analysis. Using E and H values from the first two columns (Cook and Pharr, 1990), yield stress values are calculated from Eq. (14). Clearly, these values are in good agreement with the results of Zeng et al. (1996) and therefore, the proposed relationship between hardness, Young's modulus and yield stress seems to be appropriate.

4.4. Brittleness

The concept of brittleness measure has been widely used in the literature for defining the brittle nature and fracture characteristics of materials. Although the concept was originally developed to define the
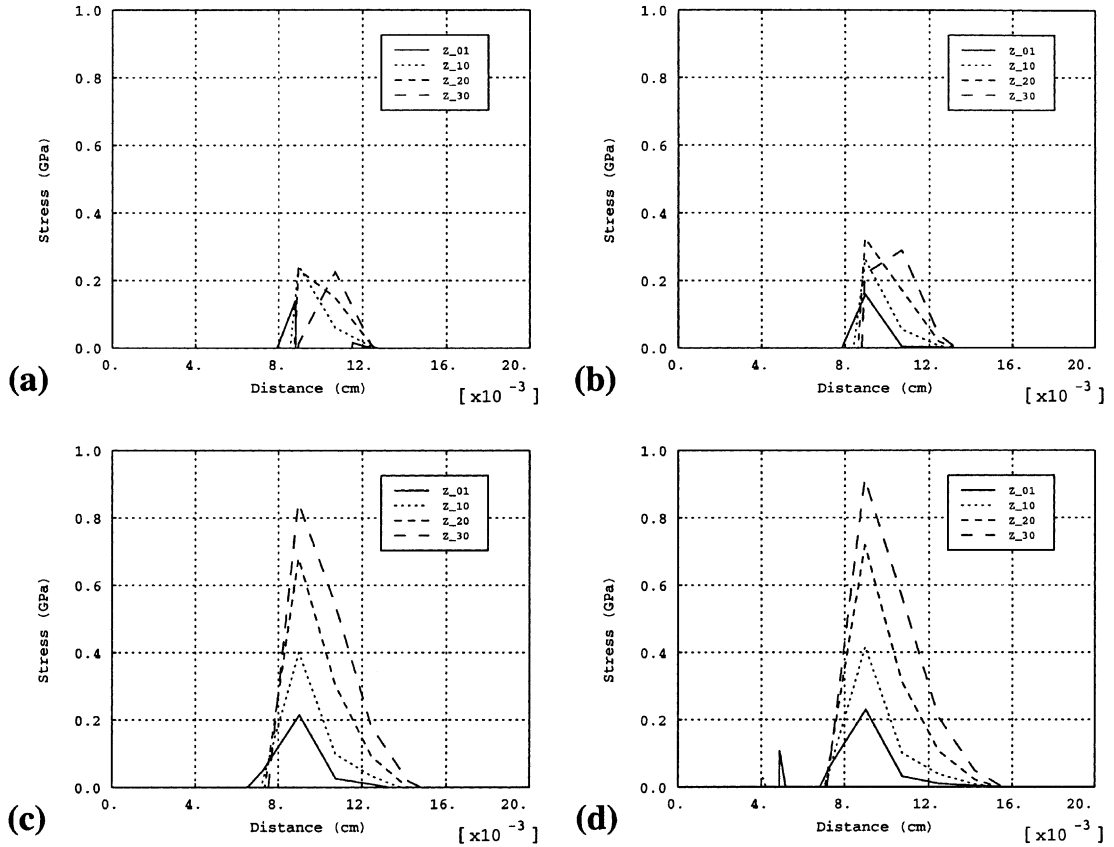
Fig. 12. Tensile stresses on planes $z = -1, -10, -20, -30$ μm at (a) 1.5, (b) 1.8, (c) 2.1 and (d) 2.4 μs.

cleavage planes in single crystals, with the advent of fracture mechanics, several new parameters have been included to characterize the brittleness of elastic solids. An in depth description of various definitions for brittleness proposed in the literature were recently reviewed by Quinn and Quinn (1997). One of the widely used definitions that is of relevance to this work is

$$B = \frac{EH_c}{K_{IC}^2} = \frac{H_c}{G_{IC}} = \frac{H_c}{2\gamma_f}, \tag{16}$$

where B is the brittleness parameter, H_c is a measure of hardness related to work per unit volume of deformation, K_{IC} is fracture toughness, G_{IC} is critical strain energy release rate and γ_f is the fracture surface energy. Note that brittleness is not directly related to hardness but includes deformation energy (Quinn and Quinn, 1997). The roles of various parameters in the above definition of B are simple to comprehend. When E and H_c are high, the material is more resistant to deformation and hence the concentrated stresses due to a point load are not easily distributed over a larger volume, thus leading to easy material fracture. On the other hand, low fracture toughness or low fracture surface energy correspond to high brittleness.
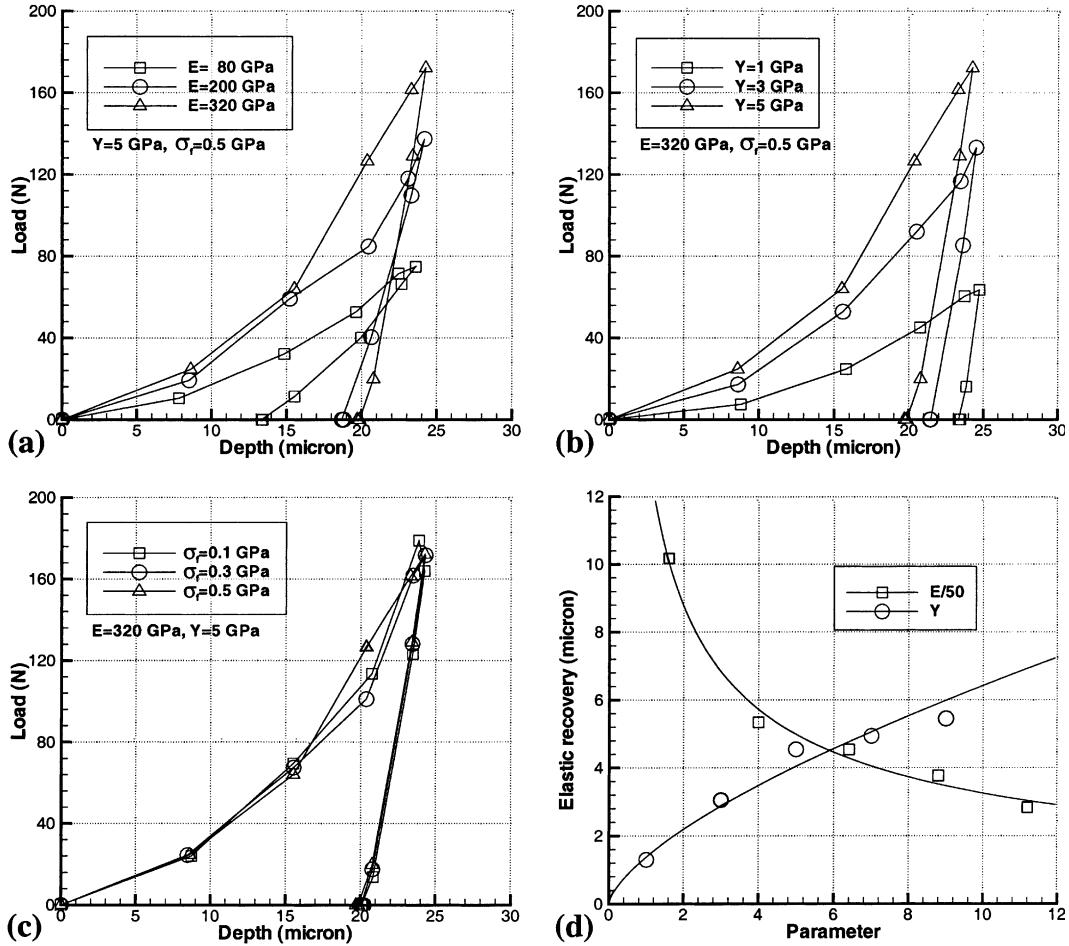
Fig. 13. Influence of (a) Young's modulus, (b) yield stress, and (c) fracture stress on P–h curves during the Vickers indentation cycle. (d) Plot of elastic recovery as a function of material properties.

The disadvantage of the above brittleness measure is that, parameters such as H_c are not mechanistic measures and cannot be directly used in computational codes. Therefore, in this work, a measure that includes material properties such as E, Y and σ_f which can be easily obtained from simple tests, were used to define the brittleness. The material properties in Table 1 were systematically varied over a wide range ($80 \leqslant E \leqslant 560$, $1 \leqslant Y \leqslant 9$, $0.1 \leqslant \sigma_f \leqslant 0.9$ GPa) to investigate the size of the induced damage zone due to indentation in brittle materials. The analysis indicated that although B is proportional to EY/σ_f^2, when median and lateral damage zone sizes were plotted against the parameter $(EY/\sigma_f^2)^{1/3}$, linear relationships were noticed as illustrated in Fig. 16. This implies that the above quantity can reflect the brittleness of a material and therefore, we define brittleness as

$$B = (EY/\sigma_f^2)^{1/3}. \tag{17}$$

Unlike the definition of Quinn and Quinn (1997) for brittleness (Eq. (16)) which has the units of length^{-1}, the current definition in Eq. (17) yields a non-dimensional number. To better visualize the usefulness of this
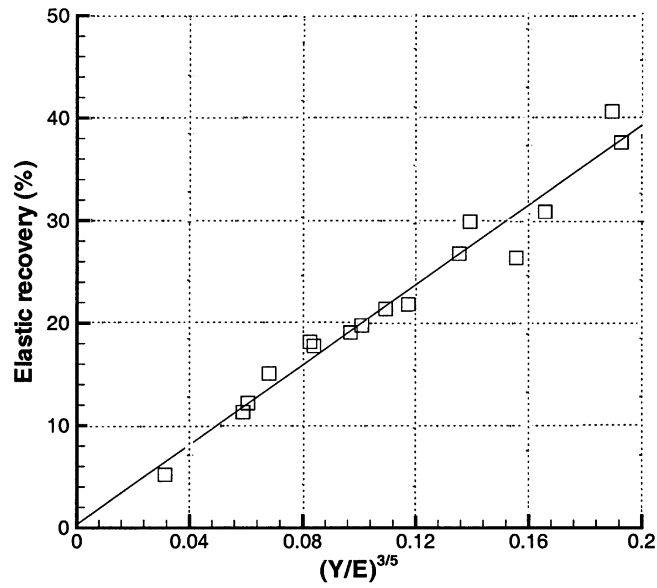
Fig. 14. Elastic recovery versus parameter $(Y/E)^{3/5}$.
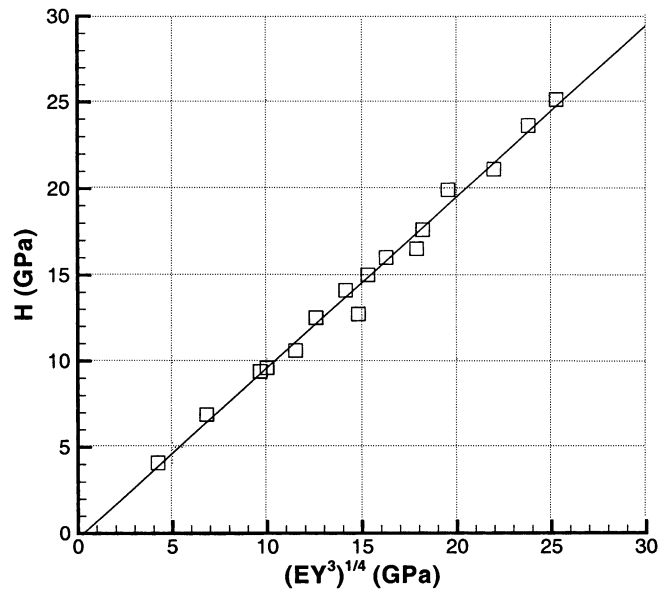
Fig. 15. Hardness versus parameter $(EY^3)^{1/4}$.

parameter, brittleness values for several ceramics are presented in Table 3 from the available data in the literature (the value of yield stress for Eq. (17) was estimated from Eq. (16), i.e., $Y = (H^4/E)^{1/3}$). It is interesting to see that although the collected data from various sources is dependent on test method, sample

Table 2
Relationship between hardness, Young's modulus and yield stress

Material	E (GPa)[a]	H (GPa)[a]	H' (GPa)[b]	Y' (GPa)[b]	$Y = (H^4/E)^{1/3}$ (GPa)
SLS-glass	70	5.9	5.84	2.8	2.59
AS-glass	91	6.6	6.40	3.2	2.75
Fused silica	72	6.3	6.32	3.0	2.80
BS-glass	89	6.5	6.30	3.0	2.72
Al_2O_3	393	21.8	20.87	10.0	8.31
$Y-ZrO_2$	220	17.8	16.74	8.1	7.70
MgO	305	7.7	7.72	3.7	2.26
$MgAl_2O_4$	293	13.1	12.90	6.3	4.65
$SrTiO_3$	292	5.0	4.89	2.4	1.29
SrF_2	88	1.4	1.37	0.4	0.35
CaF_2	110	1.9	1.70	0.6	0.49

[a] Cook and Pharr (1990).
[b] Zeng et al. (1996).
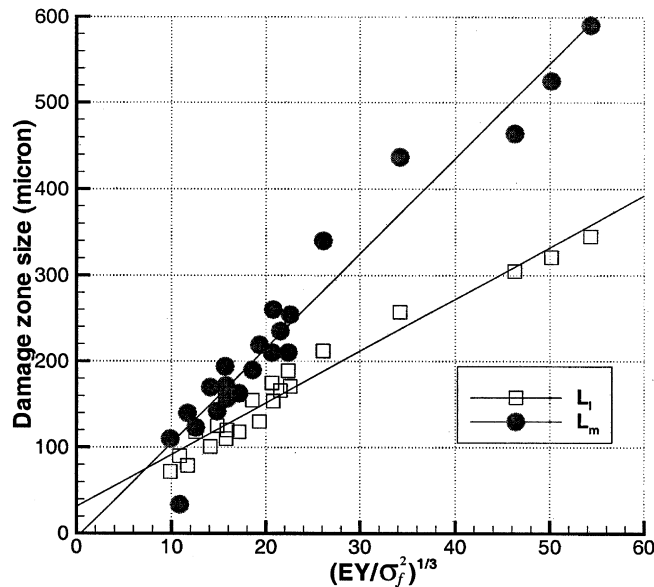
Fig. 16. Plot of damage zone size versus brittleness parameter $(EY/\sigma_f^2)^{1/3}$.

preparation and sample size, the relative trends in brittleness observed for given set of ceramics are the same in majority of situations. For ceramics that exhibit no plasticity, the brittleness value is considerably higher than those ceramics that exhibit transformation plasticity (e.g. partially stabilized zirconia). Therefore, the use of current definition (Eq. (17)) for brittleness seems to be reasonable.

5. Conclusions

An elastic–plastic-cracking model that accounts for tensile cracking and compressive yielding in brittle materials is developed and successfully implemented in ABAQUS explicit FE code. The model was used to

Table 3
Brittleness values for typical brittle materials

Ceramic	E (GPa)	Y (MPa)	σ_f (MPa)	H (GPa)	K_{IC} (MPa$\sqrt{m}$)	$[EY/\sigma_f^2]^{1/3}$	EH/K_{IC}^2 (µm^{-1})	Reference
PSZ	205	3557	350	9.8	8.5	18.1	27.8	[a]
Si_3N_4	310	5321	375	14.7	6.1	22.7	122.5	[b]
Al_2O_3	390	5154	310	15.2	4.5	27.6	292.7	[c]
SiC	440	9356	335	24.5	5.2	33.2	398.7	[d]
TiB_2	550	9643	275	26.5	5.0	41.2	583.0	[d]
MgO	305	2259	97	7.7	1.2	41.8	1630.9	[e]
B_4C	445	11349	155$_{(980°)}$	28.4	3.5	59.5	1031.7	[d]

[a] Murray (1997).
[b] Murray (1997); Bauccio (1994); Shackelford (1994).
[c] ASM (1989); Bauccio (1994).
[d] Murray (1997); Bauccio (1994).
[e] Bauccio (1994); Shackelford (1994); Schneider (1991).

simulate the fracture characteristics of brittle materials subjected to Vickers indentation. The simulation results revealed that the model is capable of capturing various crack systems that evolve in brittle materials during a Vickers indentation cycle. Similar to the experimental observations, the model predicted evolution of median cracks during the loading phase and lateral cracks during the unloading phase. This was achieved through introduction of plasticity in the constitutive behavior. The brittle material was allowed to yield during the loading phase thus creating an irreversible plastic zone beneath the indentation. Upon unloading, the mismatch in elastic and plastic deformation resulted in large tensile stress development thus resulting in lateral crack development. This phenomenon could not be captured using other models where plasticity was excluded. The introduction of plasticity can also remove stress intensity at sharp edges of the Vickers indenter which otherwise can lead to numerical instability during computation.

The model predictions of *P–h* relationship agree well with the experimental trends on typical glasses and ceramics. The elastic recovery during the unloading phase of the indentation cycle has been found to be strongly influenced by the Young's modulus and yield stress of a material, and independent of the fracture stress. Finally, the relationship between hardness and material properties of ceramics has been analyzed. It was found that a linear relationship exists between the hardness and the parameter $(EY^3)^{1/4}$.

The evolved damage zone size in a brittle material was analyzed by defining a non-dimensional brittleness parameter $(EY/\sigma_f^2)^{1/3}$, which was found to correlate linearly with the induced damage zone size. Since the fracture stress is squared in the denominator, it affects the crack size (or induced damage zone size) more strongly than Young's modulus and yield stress for similar increases. The above brittleness parameter also seems to quantify the susceptibility of a ceramic to brittle cracking as evidenced by the available data in the literature.

There are some limitations to the proposed EPC model. The major limitation of the model was that after the first crack is initiated at a given material point, the 'fixed orthogonal crack model' does not allow cracks to initiate in any direction other than the directions perpendicular to the first crack. Therefore, the model allows the normal stress to exceed fracture stress in those directions other than the three crack normals. This situation can be avoided by utilizing more complex models such as 'multiple-plane cracking model' (Espinosa and Brar, 1995). Another limitation is that, the available post processor in ABAQUS could not show the directions of cracks. The measured damage zone sizes were interpreted as median and lateral cracks solely based on the observed development of damage zones in a particular direction. Cook and Pharr (1990) identified the crack systems that evolve due to indentation into five categories: lateral cracks, median cracks, radial cracks, cone cracks and half-penny cracks. The EPC model is incapable of providing enough information to precisely classify the observed damage zones into any of the above categories. Therefore, the

use of the terms such as median and lateral cracks was solely subjective and should be interpreted cautiously.

Acknowledgements

Appendix A

Let γ^e be the elastic shear strain and γ^c be the cracking shear strain. Then the shear stress τ can be written as

$$\tau = \mu\gamma^e = D\gamma^c = G(\gamma^e + \gamma^c), \tag{A.1}$$

where, μ, D and G are bulk shear moduli corresponding to elastic strain, cracking strain and combined strain $(\gamma^e + \gamma^c)$, respectively. From Eq. (A.1), we can write

$$\frac{1}{G} = \frac{1}{\mu} + \frac{1}{D}. \tag{A.2}$$

Let G_1 be the local shear modulus when only crack 1 exists. Assume G_1 can be written as μ multiplied by factor f_1, i.e.,

$$G_1 = \mu f_1. \tag{A.3}$$

From Eqs. (A.2) and (A.3), we can obtain

$$\frac{1}{D_1} = \frac{1}{\mu f_1} - \frac{1}{\mu}. \tag{A.4}$$

Similarly, if only crack 2 exists, we can write

$$\frac{1}{D_2} = \frac{1}{\mu f_2} - \frac{1}{\mu}. \tag{A.5}$$

If both crack 1 and crack 2 exist, total crack shear strain γ^c_{12} can be written as

$$\gamma^c_{12} = \gamma^c_1 + \gamma^c_2, \tag{A.6}$$

which yields the following relationship as per Eq. (A.1)

$$\frac{1}{D_{12}} = \frac{1}{D_1} + \frac{1}{D_2}. \tag{A.7}$$

Solving Eqs. (A.2), (A.4), (A.5) and (A.7) for G (corresponding to D_{12}) yields

$$G = \frac{\mu f_1 f_2}{f_1 + f_2 - f_1 f_2}. \tag{A.8}$$

Generalizing above equation, we have

$$G = \frac{\mu f_i f_j}{f_i + f_j - f_i f_j}. \tag{A.9}$$

By denoting the plastic shear strain γ_{ij}^{p}, total strain can be written as

$$\gamma_{ij} = \gamma_{ij}^{\mathrm{e}} + \gamma_{ij}^{\mathrm{c}} + \gamma_{ij}^{\mathrm{p}}. \tag{A.10}$$

Hence, shear stress t_{ij} can be calculated as

$$t_{ij} = G(\gamma_{ij} - \gamma_{ij}^{\mathrm{p}}) = 2G(e_{ij} - e_{ij}^{\mathrm{p}}). \tag{A.11}$$

References

ABAQUS Theory Manual, Version 5.8, Hibbitt, Karlsson and Sorensen, 1998a.

ABAQUS/Explicit User Manual, Version 5.8, Hibbitt, Karlsson and Sorensen, 1998b.

Ahn, Y., Farris, T.N., Chandrasekar, S., 1998. Sliding microindentation fracture of brittle materials: role of elastic stress fields. Mech. Mater. 29, 143–152.

ASM Engineered Materials Reference Book, 1989. ASM international, Metals Park, Ohio.

Anton, R.J., Subhash, G., 2000. Dynamic Vickers indentation of brittle materials. Wear 239, 27–35.

Bauccio, M. (Ed.), 1994. ASM Engineering Materials Reference Book, second edition. ASM International, Metals Park, Ohio.

Bhattacharya, A.K., Nix, W.D., 1988. Finite element simulation of indentation experiments. Int. J. Solids Struct. 24 (9), 881–891.

Care, G., Fischer-Cripps, A.C., 1997. Elastic–plastic indentation stress fields using the finite-element method. J. Mater. Sci. 32 (21), 5653–5659.

Chiang, S.S., Marshall, D.B., Evans, A.G., 1982. The response of solids to elastic/plastic indentation. I. Stresses and residual stresses. J. Appl. Phys. 53 (1), 298–311.

Chow, C.L., Liu, Y.J., Asundi, A., 1993. An incremental stress-based constitutive modeling on anisotropic damaged materials. Int. J. Fract 64, 299–319.

Cook, R.F., Pharr, G.M., 1990. Direct observation and analysis of indentation cracking in glasses and ceramics. J. Am. Ceram. Soc. 73 (4), 787–817.

Espinosa, H.D., Brar, N.S., 1995. Dynamic failure mechanisms of ceramic bars: experiments and numerical simulations. J. Mech. Phys. Solids 43 (10), 1615–1638.

Fischer-Cripps, A.C., 1997. Elastic–plastic behaviour in materials loaded with a spherical indenter. J. Mater. Sci. 32, 727–736.

Giannakopoulos, A.E., Larsson, P.-L., Vestergaard, R., 1994. Analysis of Vickers indentation. Int. J. Solids Struct. 31 (19), 2679–2708.

Inasaki, I., 1986. High efficiency grinding of advanced ceramics. Annals of CIRP 35 (1), 211–214.

Koeppel, B.J., Subhash, G., 1999. Characteristics of residual plastic zone under static and dynamic indentations. Wear 224, 56–67.

Lankford, J., Predebon, W.W., Staehler, J.M., Subhash, G., Pletka, B.J., Anderson, C.E., 1998. The role of plasticity as a limiting factor in the compressive failure of high strength ceramics. Mech. Mater. 29, 205–218.

Larsson, R., 1995. A generalized fictitious crack model based on plastic localization and discontinuous approximation. Int. J. Numer Meth Engng. 38, 3167–3188.

Larsson, P.-L., Giannakopoulos, A.E., Soderlund, E., Rowcliffe, D.J., Vestergaard, R., 1996. Analysis of Berkovich indentation. Int. J. Solids Struct. 33 (2), 221–248.

Lawn, B.R., Evans, A.G., Marshall, D.B., 1980. Elastic/plastic indentation damage in ceramics. The median/radial crack system. J. Am. Ceram. Soc. 63, 574–581.

Lawn, B.R., Howes, V.R., 1981. Elastic recovery at hardness indentations. J. Mater. Sci. 16 (10), 2745–2752.

Liaw, B.M., Kobayashi, A.S., Emery, A.F., 1984. An elastic failure model of indentation damage. Mater. Sci. Res. 18, 709–722.

Marsh, D.M., 1964. Plastic flow in glass. Proc. Roy. Soc. A. 279, 420–435.

Marx, V., Balke, H., 1997. A critical investigation of the unloading behavior of sharp indentation. Acta Mater. 45 (9), 3791–3800.

McClintock, F.A., Argon, A.S., 1966. Mechanical behavior of materials. Addison-Wesley, Redding, MA, USA.

Murray, G.T. (Ed.), 1997. Handbook of Materials Selection for Engineering Applications. California Polytechnic State University San Luis Obispo, California.

Ponton, C.B., Rawlings, R.D., 1989a. Vickers indentation fracture toughness test: Part 1. Review of literature and formulation of standardized indentation toughness equations. Mater. Sci. Tech. 5, 865–960.

Ponton, C.B., Rawlings, R.D., 1989b. Vickers indentation fracture toughness test: Part 2. Application and critical evaluation of standardised indentation toughness equations. Mater. Sci. Tech. 5, 961–976.

Quinn, J.B., Quinn, G.D., 1997. Indentation brittleness of ceramics: a fresh approach. J. Mater. Sci. 32 (16), 4331–4346.

Schinker, M.G., Doll, W., 1982. Plasticity and fracture of inorganic glasses in high speed grinding. Fifth International Conference on Physics of Non-Crystalline Solids, Montpellier, France.

Schneider, S.J. Jr. (Ed.), 1991. Engineered Materials handbook, vol. 4, Ceramics and Glasses. ASM International, Metals Park, Ohio.

Shackelford, J.F. (Ed.), 1994. CRC Materials Science and Engineering Handbook. CRC Press, Boca Raton.

Spur, G., Stark, C., Tio, T.H., 1985. Grinding of non-oxide ceramics using diamond grinding wheels. Machining of Ceramic Materials and Components, PED-vol. 17, New York, pp. 33–44.

Subhash, G., Nemat-Nasser, S., 1993. Dynamic stress-induced transformation and texture formation in uniaxial compression of zirconia ceramics. J. Am. Ceram. Soc. 76 (1), 153–165.

Subramanian, K., Keat, P.P., 1985. Parametric study on grindability of structural and electronic ceramic – Part 1, in: Subramanian K., Komanduri R. (Eds.), Machining of Ceramic Materials and Components. PED-vol 17, ASME, New York, pp. 25–32.

Tabor, D., 1951. The Hardness of Metals. Clarendon Press, Oxford.

Yoffe, E.H., 1982. Elastic stress fields caused by indenting brittle materials. Philos. Mag. A 46, 617–628.

Yu, C.T., Kobayashi, A.S., 1993. Fracture process zone in SiC_w/Al_2O_3. Ceram. Engng. Sci. Proc. 14 (7), 273–281.

Zeng, K., Soderlund, E., Giannakopoulos, A.E., Rowcliffe, D.J., 1996. Controlled indentation: A general approach to determine mechanical properties of brittle materials. Acta Mater. 44 (3), 1127–1141.

Zhang, L., Mahdi, M., 1996. The plastic behaviour of silicon subjected to micro-indentation. J. Mater. Sci. 31, 5671–5676.